Thermal Transport Model of a Sorbent Particle Undergoing Calcination–Carbonation Cycling

Lindsey Yue and Wojciech Lipiński
Research School of Engineering, The Australian National University, Canberra, ACT 2601, Australia

DOI 10.1002/aic.14840
Published online May 7, 2015 in Wiley Online Library (wileyonlinelibrary.com)

A numerical model coupling transient radiative, convective, and conductive heat transfer, mass transfer, and chemical kinetics of heterogeneous solid–gas reactions has been developed for a semitransparent, nonuniform, and nonisothermal particle undergoing cyclic thermochemical transformations. The calcination–carbonation reaction pair for calcium oxide looping is selected as the model cycle because of its suitability for solar-driven carbon dioxide capture. The analyzed system is a single, porous particle undergoing thermochemical cycling in an idealized, reactor-like environment. The model is used to investigate two cases distinguished by the length of the calcination and carbonation periods. The calcination–carbonation process for a single particle is shown to become periodic after three cycles. © 2015 American Institute of Chemical Engineers *AIChE J*, 61: 2647–2656, 2015
Keywords: thermochemistry, porous media, concentrated solar, CO_2 capture

Introduction

Thermochemical cycles are found in important industrial applications, including thermal energy storage, chemical-looping combustion, and the production of commodity materials. Calcium oxide looping is a thermochemical cycle of recent interest for carbon dioxide (CO_2) capture.[1] The cycle is well suited for use with concentrated solar irradiation.[2] The high-temperature capture of CO_2 via solar calcium oxide looping promises high efficiencies and capture rates.[3] Concentrated CO_2 is a commodity with applications in the pharmaceutical, medical, environmental, food and beverage, petrochemical, oil recovery, metallurgy, and manufacturing industries,[4,5] as well as the production of synthetic transportation fuels.[6,7]

In the first step of calcium oxide looping, calcium carbonate ($CaCO_3$) is thermochemically decomposed into concentrated CO_2 and calcium oxide (CaO) in the endothermic, solar-driven calcination reaction

$$CaCO_3 \rightarrow CaO + CO_2, \quad \Delta\bar{h}^0_{298\,K} = 178\,kJ\,mol^{-1} \qquad (1)$$

In the second step, CO_2 is chemically absorbed from a dilute source by CaO to form $CaCO_3$ in the exothermic, non-solar carbonation reaction

$$CaO + CO_2 \rightarrow CaCO_3, \quad \Delta\bar{h}^0_{298\,K} = -178\,kJ\,mol^{-1} \qquad (2)$$

In a systems for calcium oxide looping, intraparticle heat transfer, mass transfer, and chemical kinetics are all important considerations. The intraparticle phenomena were studied using numerical models of heat and mass transfer coupled to calcination chemical kinetics.[8–12] Previous pertinent studies dealt with radiation and other heat transfer characteristics of reacting particles,[13–15] interaction of particles with high-flux solar irradiation,[16] chemical kinetics of both the calcination[17,18] and carbonation[3,19–21] reactions, intraparticle mass transfer effects on kinetics,[22–24] and sorbent degradation.[25,26]

This research aims at understanding the role of transport processes in the complete, two-step calcium oxide looping cycle for CO_2 capture driven by concentrated solar irradiation. It extends the chemical kinetics model and consequently, the transient thermal transport model previously developed[12] to the full calcination–carbonation cycle. A solar reactor for the implementation of the calcination–carbonation cycle is currently under development.[27]

Problem Statement

The model system is a single, semitransparent, porous particle with nonuniform composition and temperature undergoing thermochemical cycling in a reactor-like environment shown in Fig. 1. The system to be analyzed consists of two solid-phase species ($CaCO_3$ and CaO) and two fluid-phase species (CO_2 and air). The particle is thermochemically cycled by alternately being exposed to concentrated irradiation to drive the endothermic reaction and allowed to passively cool to favor the exothermic reaction.

The local, intrinsic chemical reaction rate depends on temperature, solid phase composition, CO_2 concentration, and particle morphology. Fluid in the pore space moves due to species diffusion and bulk advection. Convective mass transfer occurs at the particle surface to the surrounding fluid. In the heat transfer model, conduction is modeled in both the solid and fluid phases. The solid phase is radiatively participating while the fluid phase is radiative nonparticipating. Convective heat transfer occurs between both phases and the surrounding fluid at the particle surface. Radiative heat

Correspondence concerning this article should be addressed to W. Lipiński at wojciech.lipinski@anu.edu.au.

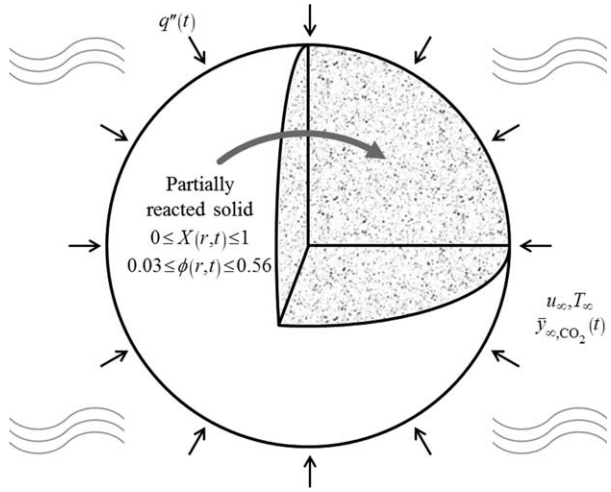

Figure 1. A single particle in a reactor-like environment with nonuniform composition and temperature.

transfer occurs between the particle surface and the surrounding reactor walls. Ambient conditions and incident irradiation are assumed to be uniform over the particle surface. Physical properties are assumed to be independent of the polar and azimuthal coordinates.

Governing Equations

The numerical model consists of five volume-averaged, governing conservation equations; four conservation of mass equations for the four species of the system and one conservation of energy equation. Constraint equations include a simplified conservation of momentum equation and the ideal gas equation of state.

To properly resolve time-dependent composition and temperature profiles within the particle during cycling, mass, momentum, and energy equations have been included in the model. Single global time-dependent conversion expressions, without solving for intraparticle composition or temperature profiles, have been developed for the calcination[28,29] and carbonation[19,30] reactions. However, they have limited applicability as they are specific to experimental conditions and do not account for mass diffusion limitations. Conversion limits due to diffusion have been experimentally shown to occur in carbonating particles.[31] Governing equations for the local solid phase composition, fluid phase composition, and temperature are included in the numerical model, because these quantities influence the local intrinsic kinetics of the calcination[22,24] and carbonation[20,21] reactions.

Conservation of mass—solid phase

The volume-averaged conservation of mass equations for $CaCO_3$ and CaO read, respectively

$$\frac{\partial\left[(1-\phi)\langle\bar{\rho}_{\mathrm{CaCO_3}}\rangle^{\mathrm{s}}\right]}{\partial t}=\langle\bar{r}'''\rangle \tag{3}$$

$$\frac{\partial\left[(1-\phi)\langle\bar{\rho}_{\mathrm{CaO}}\rangle^{\mathrm{s}}\right]}{\partial t}=-\langle\bar{r}'''\rangle \tag{4}$$

where the reaction rate term on the right-hand side is defined as

$$\bar{r}''' \overset{\mathrm{def}}{=} -\frac{\mathrm{d}N_{\mathrm{CaCO_3}}}{\mathrm{d}V\mathrm{d}t}=\frac{\mathrm{d}N_{\mathrm{CaO}}}{\mathrm{d}V\mathrm{d}t}=\frac{\mathrm{d}N_{\mathrm{CO_2}}}{\mathrm{d}V\mathrm{d}t} \tag{5}$$

$N_{\mathrm{CaCO_3}}$, N_{CaO}, and $N_{\mathrm{CO_2}}$ are the local amounts of substance of $CaCO_3$, CaO, and CO_2, respectively. As the solid phase composition changes, concomitant changes in porosity ϕ are considered, but the particle radius r_{p} is assumed constant.

Conservation of mass—fluid phase

For the fluid phase, the volume-averaged conservation of mass equations for CO_2 and air read, respectively

$$\frac{\partial\left(\phi\langle\bar{\rho}_{\mathrm{CO_2}}\rangle^{\mathrm{f}}\right)}{\partial t}+\nabla\cdot\left(\langle\bar{\rho}_{\mathrm{CO_2}}\rangle^{\mathrm{f}}\langle\overrightarrow{u_{\mathrm{f}}}\rangle\right)=\nabla\cdot\left(D_{\mathrm{CO_2,eff}}\nabla\langle\bar{\rho}_{\mathrm{CO_2}}\rangle^{\mathrm{f}}\right)+j''_{\mathrm{CO_2}}s'''_{\mathrm{phase}} \tag{6}$$

$$\frac{\partial\left(\phi\langle\bar{\rho}_{\mathrm{air}}\rangle^{\mathrm{f}}\right)}{\partial t}+\nabla\cdot\left(\langle\bar{\rho}_{\mathrm{air}}\rangle^{\mathrm{f}}\langle\overrightarrow{u_{\mathrm{f}}}\rangle\right)=\nabla\cdot\left(D_{\mathrm{air,eff}}\nabla\langle\bar{\rho}_{\mathrm{air}}\rangle^{\mathrm{f}}\right) \tag{7}$$

where the molar concentrations of CO_2 and air change due to bulk advection, species diffusion, and for CO_2, chemical reaction and transport across the solid–fluid phase boundary. All pores are assumed active and connected to the particle exterior. Air is modeled as a single species composed of 79% nitrogen and 21% oxygen. Closure equations for bulk advection and diffusion are formulated using molar-averaged effective properties.[12]

Conservation of momentum

Darcy's law simplification of the conservation of momentum equation is used to determine the fluid velocity in the pore space. Darcy's law simplification is used for its simplicity and appropriateness,[32] because fluid velocities are low enough to maintain laminar flow at all times and locations within the particle

$$-\nabla\left(\phi\langle p_{\mathrm{f}}\rangle^{\mathrm{f}}\right)=\frac{\mu_{\mathrm{f}}}{K}\phi\langle\overrightarrow{u_{\mathrm{f}}}\rangle \tag{8}$$

where p_{f} is the local fluid pressure, μ_{f} is the viscosity of the fluid, K is the permeability of the porous solid, and $\langle\overrightarrow{u_{\mathrm{f}}}\rangle$ is the superficial fluid velocity. The local fluid pressure is evaluated using the ideal gas equation as the total fluid pressure remains low at all times and locations within the particle.

Conservation of energy

The solid and fluid phases are assumed to be at local thermal equilibrium, yielding one conservation of energy equation for the system

$$\frac{\partial\langle\bar{\rho}\rangle\langle\bar{h}\rangle}{\partial t}+\nabla\cdot\left(\langle\bar{\rho}_{\mathrm{f}}\rangle^{\mathrm{f}}\langle\bar{h}_{\mathrm{f}}\rangle^{\mathrm{f}}\langle\overrightarrow{u_{\mathrm{f}}}\rangle\right)=\nabla\cdot\left(\langle\bar{h}_{\mathrm{CO_2}}\rangle^{\mathrm{f}}D_{\mathrm{CO_2,eff}}\nabla\langle\bar{\rho}_{\mathrm{CO_2}}\rangle^{\mathrm{f}}\right)+\nabla\cdot\left(\langle\bar{h}_{\mathrm{air}}\rangle^{\mathrm{f}}D_{\mathrm{air,eff}}\nabla\langle\bar{\rho}_{\mathrm{air}}\rangle^{\mathrm{f}}\right)+\nabla\cdot\left(k_{\mathrm{eff}}\nabla\langle T\rangle\right)-\langle\nabla\cdot\overrightarrow{q}''_{\mathrm{rad}}\rangle \tag{9}$$

where latent heat changes due to bulk fluid advection, fluid species diffusion, conduction, and radiative heat transfer within the particle. Property relations for enthalpy and equations for effective conductivity and radiative heat flux used in Eq. 9 have been previously reported.[12]

Initial and boundary conditions

The particle is initially 100% $CaCO_3$, so the cycle starts with a calcination period followed by a carbonation period. One calcination period t_{calc} and one carbonation period t_{carb} comprise one cycle $t_{\mathrm{cycle}}=t_{\mathrm{calc}}+t_{\mathrm{carb}}$. A cycle j begins with a

calcination period at time instant t_j, and the carbonation period for cycle j begins at time instant $t_{j,\mathrm{calc}}=t_j+t_{\mathrm{calc}}$. The fluid in the pore space initially has the same composition as the surrounding fluid with no pressure or species concentration gradients. The particle temperature is initially at convective and radiative equilibrium with the surroundings. The surroundings are assumed black and at a uniform and constant temperature T_{w}.

Time-periodic conditions of the surrounding environment employed in the model drive thermochemical cycling. There are two time-periodic environment variables that interact with the system at the boundary: the surrounding CO_2 concentration and the incident irradiation. CO_2 is absorbed from a dilute source and released in a concentrated stream. Therefore for calcination, the surrounding fluid is modeled as a stream of commodity-grade concentrated CO_2 with non-CO_2 impurities modeled as air. For carbonation, the surrounding fluid is modeled as a mixture of air and CO_2 with the CO_2 concentration representative of coal-fired flue gas

$$\bar{y}_{\infty,\mathrm{CO_2}}=\begin{cases}\bar{y}_{\mathrm{CO_2,calc}} & \text{for } 0<t-t_j\le t_{\mathrm{calc}}\\ \bar{y}_{\mathrm{CO_2,carb}} & \text{for } t_{\mathrm{calc}}<t-t_j\le t_{\mathrm{cycle}}\end{cases} \tag{10}$$

where $\bar{y}_{\infty,\mathrm{CO_2}}$ is the surrounding CO_2 concentration, $\bar{y}_{\mathrm{CO_2,calc}}$ is the calcination CO_2 concentration, and $\bar{y}_{\mathrm{CO_2,carb}}$ is the carbonation CO_2 concentration.

During the calcination period, high-flux solar irradiation drives particle heating and endothermic calcination. The incident solar irradiation is diffuse and distributed uniformly over the particle surface. During the carbonation period, the particle cools by reradiation and convection to allow exothermic carbonation. The external heat flux at the particle surface varies periodically with time according to

$$q''_{\mathrm{surf}}=\begin{cases}q''_{\mathrm{solar}} & \text{for } 0<t-t_j\le t_{\mathrm{calc}}\\ 0 & \text{for } t_{\mathrm{calc}}<t-t_j\le t_{\mathrm{cycle}}\end{cases} \tag{11}$$

where q''_{solar} is the magnitude of the concentrated solar radiation. The transition between periods for both conditions in Eqs. 10 and 11 occurs as a step change. Values of the parameters used in Eqs. 10 and 11 are given in Table 1.

The time-periodic surrounding environment variables drive thermochemical cycling within the system through the boundary conditions for the fluid phase conservation of mass equations and the conservation of energy equation. The boundary conditions for Eqs. 6 and 7 read

$$\left[\langle\bar{\rho}_i\rangle^{\mathrm{f}}\langle\vec{u}_{\mathrm{f}}\rangle-D_{i,\mathrm{eff}}\frac{\partial\langle\bar{\rho}_i\rangle^{\mathrm{f}}}{\partial r}\right]_{r=r_{\mathrm{p}}}=h_{\mathrm{m,eff}}\left(\langle\bar{\rho}_i\rangle^{\mathrm{f}}|_{r=r_{\mathrm{p}}}-\bar{\rho}_{\infty,i}\right) \tag{12}$$

$$\left.\frac{\partial\langle\bar{\rho}_i\rangle^{\mathrm{f}}}{\partial r}\right|_{r=0}=0 \tag{13}$$

Table 1. Selected Boundary and Initial Conditions

Variable	Value	Unit
q''_{solar}	235	kW m^{-2}
$\bar{y}_{\mathrm{CO_2,calc}}$	0.99	
$\bar{y}_{\mathrm{CO_2,carb}}$	0.15	
T_0	800	K
T_{w}	800	K
T_∞	800	K

where $i=\mathrm{CO_2}$, air. The first term on the left-hand side of Eq. 12 is the advective flux, the second term is the diffusive flux, and the remaining term on the right-hand side is the convective mass transfer between the fluid at the particle surface and the surrounding fluid. The surrounding molar densities of CO_2 and air are, respectively

$$\bar{\rho}_{\infty,\mathrm{CO_2}}=\bar{y}_{\infty,\mathrm{CO_2}}\frac{p_\infty}{\bar{R}T_\infty} \tag{14}$$

$$\bar{\rho}_{\infty,\mathrm{air}}=\left(1-\bar{y}_{\infty,\mathrm{CO_2}}\right)\frac{p_\infty}{\bar{R}T_\infty} \tag{15}$$

The boundary conditions for Eq. 9 are

$$k_{\mathrm{eff}}\left.\frac{\partial\langle T\rangle}{\partial r}\right|_{r=r_{\mathrm{p}}}=h_{\mathrm{eff}}\left(T_\infty-\langle T\rangle|_{r=r_{\mathrm{p}}}\right)+\alpha_{\mathrm{eff,solar}}q''_{\mathrm{surf}}+\alpha_{\mathrm{eff,w}}\sigma T_{\mathrm{w}}^4-\varepsilon_{\mathrm{eff,p}}\sigma\left(\langle T\rangle|_{r=r_{\mathrm{p}}}\right)^4 \tag{16}$$

$$\left.\frac{\partial\langle T\rangle}{\partial r}\right|_{r=0}=0 \tag{17}$$

The numerical model does not take into account particle degradation and loss of sorbent activity due to cycling or irreversible morphological changes such as sintering. These phenomena have been experimentally shown to occur in particles undergoing cyclic calcination and carbonation[33] and should be considered in the realization of solar calcium oxide looping CO_2 capture.

Chemical Kinetics

The volumetric reaction model is used for both calcination and carbonation. The reaction rate expressions for both reactions include Arrhenius-type rate constants, morphology factors, and CO_2 partial pressure dependence

$$\bar{r}'''=-k_{\mathrm{calc}}s'''_{\mathrm{calc}}f_{\mathrm{CO_2,calc}}+k_{\mathrm{carb}}s'''_{\mathrm{carb}}f_{\mathrm{CO_2,carb}} \tag{18}$$

$$k_i=k_{0,i}\exp\left(-E_{\mathrm{a},i}/\bar{R}T\right)\text{ for }i=\mathrm{calc,carb} \tag{19}$$

where k is the Arrhenius-like rate constant, s''' is the local, volume-specific reaction surface area, and $f_{\mathrm{CO_2}}$ is a function describing the CO_2 partial pressure dependence. The kinetic models for calcination of Blanca limestone[24] and carbonation of fully calcined Strassburg limestone[20] are used for reactions 1 and 2, respectively.

Calcination kinetics

The volume-specific reaction specific surface area for calcination is given by

$$s'''_{\mathrm{calc}}=\frac{\left[s_{\mathrm{CaCO_3}}(1-X_{\mathrm{local}})+s_{\mathrm{CaO}}X_{\mathrm{local}}\right]}{\frac{1}{(1-\phi)}\left[\frac{X_{\mathrm{local}}}{\rho_{\mathrm{CaO}}}+\frac{1-X_{\mathrm{local}}}{\rho_{\mathrm{CaCO_3}}}\right]} \tag{20}$$

where $s_{\mathrm{CaCO_3}}$ is the mass-specific surface area of unreacted, 3%-porous $CaCO_3$, s_{CaO} is the mass-specific surface area of 56%-porous CaO, and X_{local} is the local extent of the calcination reaction further referred to as the reaction extent, $X_{\mathrm{local}}=1-N_{\mathrm{CaCO_3}}/N_{0,\mathrm{CaCO_3}}$. The Langmuir–Hinshelwood mechanism model with the Freundlich isotherm was found to best predict the dependence on CO_2 partial pressure of experimental data in the temperature range 1048–1173 K.[24] The model has been extrapolated to 1200 K for use in this work

Table 2. Reaction Rate Parameters

Variable	Value	Unit	
$k_{0,\mathrm{calc}}$	6.7×10^{6}	mol m^{-2} s^{-1}	[24]
$E_{\mathrm{a,calc}}$	1.66×10^{5}	J mol^{-1}	[24]
$s_{\mathrm{CaCO_3}}$	300	m^2 kg^{-1}	[24]
s_{CaO}	1.9×10^{4}	m^2 kg^{-1}	[24]
$\rho_{\mathrm{CaCO_3}}$	2730	kg m^{-3}	
ρ_{CaO}	3350	kg m^{-3}	
$\phi_{\mathrm{CaCO_3}}$	0.03		[24]
ϕ_{CaO}	0.56		[24]
c_0	1.8×10^{-7}	Pa$^{-1/2}$	[24]
E_{c}	-9.3×10^{4}	J mol^{-1}	[24]
A_{eq}	4.137×10^{12}	Pa	[34]
B_{eq}	2.0474×10^{4}	K	[34]
$k_{0,\mathrm{carb}}$	1.67×10^{-4}	mol m^{-2} s^{-1} kPa	[20]
$E_{\mathrm{a,carb}}$	2.9×10^{4}	J mol^{-1}	[20]

$$f_{\mathrm{CO_2,calc}}=\begin{cases}(1-\theta)\left(1-\dfrac{p_{\mathrm{CO_2}}}{p_{\mathrm{eq}}}\right) & \text{for } p_{\mathrm{CO_2}}<p_{\mathrm{eq}}\\ 0 & \text{for } p_{\mathrm{CO_2}}\geq p_{\mathrm{eq}}\end{cases} \tag{21}$$

$$\theta=\begin{cases}cp_{\mathrm{CO_2}}^{1/2} & \text{for } \theta<1\\ 1 & \text{for } \theta\geq 1\end{cases} \tag{22}$$

$$c=c_0\exp\left(\frac{-E_{\mathrm{c}}}{\bar{R}T}\right) \tag{23}$$

where θ is the fraction of active sites occupied by CO_2, c is the adsorption constant, $p_{\mathrm{CO_2}}$ is the local partial pressure of CO_2, and p_{eq} is the equilibrium partial pressure of CO_2, evaluated at the local temperature

$$p_{\mathrm{eq}}=A_{\mathrm{eq}}\exp\left(-\frac{B_{\mathrm{eq}}}{T}\right) \tag{24}$$

Values of parameters used for the calcination reaction rate constant and in Eqs. 20, 23, and 24 are given in Table 2. The calcination reaction rate normalized by reaction specific surface area for selected CO_2 concentrations is shown in Figure 2a. Increasing temperature and decreasing CO_2 concentration increases the calcination rate.

Carbonation kinetics

The volume-specific reaction specific surface area for carbonation is given by

$$s'''_{\mathrm{carb}}=s_{\mathrm{CaO}}\rho_{\mathrm{CaO}}(1-\phi_{\mathrm{CaO}})X_{\mathrm{local}}^{2/3} \tag{25}$$

The CO_2 partial pressure dependence for carbonation is

$$f_{\mathrm{CO_2,carb}}=\begin{cases}p_{\mathrm{CO_2}}-p_{\mathrm{eq}} & \text{for } p_{\mathrm{CO_2}}>p_{\mathrm{eq}}\\ 0 & \text{for } p_{\mathrm{CO_2}}\leq p_{\mathrm{eq}}\end{cases} \tag{26}$$

Values for parameters used for the carbonation reaction rate constant and in Eq. 25 are given in Table 2. The carbonation reaction rate normalized by reaction specific surface area for selected CO_2 concentrations is shown in Figure 2b. Increasing CO_2 concentration results in faster kinetics. Increasing temperature results in faster kinetics until a maximum reaction rate for a given CO_2 concentration is reached. Further increasing temperature above the maximum reaction rate temperature results in sharply declining values until $f_{\mathrm{CO_2,carb}}=0$, and consequently zero carbonation reaction rate, is reached at the local equilibrium temperature.

The overall reaction rate is shown in Figure 3 as a function of temperature for selected CO_2 concentrations. Negative and positive rate values represent calcination and carbonation, respectively.

Numerical Solution

The governing equations are solved numerically in space and time by employing the finite volume method in one dimension and the explicit Euler time-integration scheme. In the finite volume method, the central difference scheme is used to evaluate first- and second-order integrals with upwinding for advective and diffusive terms in Eqs. 6, 7, and 9. The spacial domain is discretized into 30 spherical shell elements with constant thickness Δr. The discrete equations are solved using a Fortran 90 code developed for this application. Simulation parameters used for the numerical

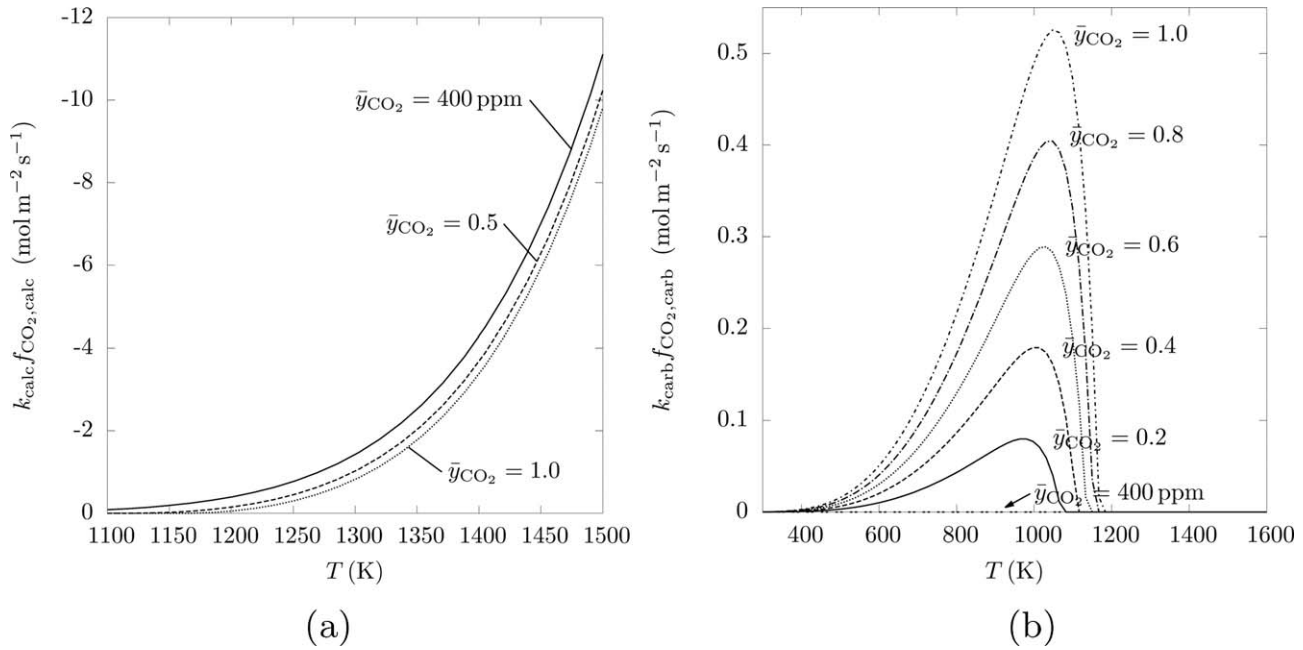

Figure 2. Reaction rate normalized by the specific surfare area vs. temperature for selected CO_2 concentrations for (a) calcination and (b) carbonation.

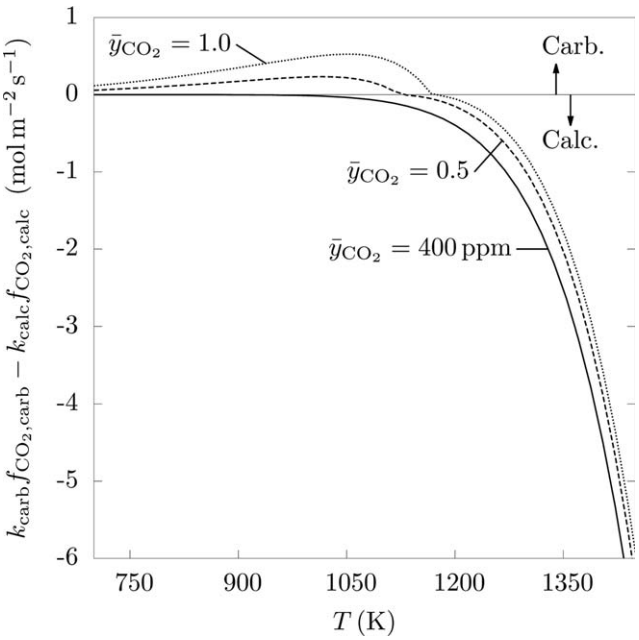

Figure 3. Overall reaction rate vs. temperature for selected CO_2 concentrations.

solution are given in Table 3. The particle has a radius of 2.5 mm. Particles of similar size have been used for pilot-scale calcium oxide looping for CO_2 capture.[35]

Results

The model is used to investigate two cases: (1) with period lengths resulting in full calcination of the particle referred to as the "full-calcination case," and (2) with period lengths resulting in full carbonation of the particle referred to as the "full-carbonation case." The period lengths for both cases have been identified in preliminary calculations using the model presented in this study.

For the full-calcination case, $t_{calc}=300\,s$ and $t_{carb}=800\,s$. The length of the calcination period is determined by the time it takes to completely calcine the particle. Once complete calcination is achieved, the carbonation period begins. The particle carbonates until the end of the carbonation period at which time the cycle ends and the next cycle begins with another calcination period. In the full-calcination case, the particle does not completely carbonate during the first or subsequent carbonation periods.

For the full-carbonation case, $t_{calc}=30\,s$ and $t_{carb}=190\,s$. The length of the calcination period is determined by the maximum extent of calcination which allows for full carbonation during the carbonation period. The calcination period proceeds until this maximum extent of calcination is reached. Then the carbonation period begins, and the particle carbonates until full carbonation is achieved and the next cycle starts.

Table 3. Numerical Solution Parameters

Variable	Value	Unit
Particle radius r_p	0.0025	m
Nodes	30	–
Time step Δt	2×10^{-6}	s
Ambient total pressure p_∞	101, 325	Pa
Free stream velocity u_∞	0.09	m s^{-1}

Six cycles were simulated for both cases. After two cycles, periodicity is achieved, and the third and subsequent cycles for both cases are identical. All physical and numerical simulation parameters are taken from Ref. 12 with the exception of parameters in Tables 1 and 3 as discussed in the preceding sections.

Full-calcination case

Overall reaction extent, $X_{overall}=1-N_{CaCO_3,p}/N_{0,CaCO_3,p}$, vs. time for the full-calcination case is shown in Figure 4. Figure 4a shows all six cycles, and Figure 4b shows cycle $j=4$. At $t=0\,s$, $X_{overall}=0$, and the cycle starts with a calcination period. The particle heats to the calcination temperature and begins decomposing into CaO and CO_2 at $t=6\,s$ for the first cycle and at $t=t_j+5\,s$ for subsequent cycles. Calcination continues until all $CaCO_3$ is consumed: $X_{overall}=1$ at $t=271\,s$ for the first cycle and $t=t_j+98\,s$ in subsequent cycles.

During the carbonation period, the particle cools until the carbonation temperature is reached, and the particle begins to carbonate at $t=302\,s$ for the first cycle and at $t=t_{j,calc}+2\,s$ in subsequent cycles. The particle does not completely carbonate during the first or subsequent carbonation periods, reaching a minimum overall reaction extent $X_{overall}=0.397$.

During the carbonation period, two regimes are observed. The regimes are shown in Figure 4b. The change in particle composition during the first regime, $t_{j,calc} < t-t_j < t_{j,calc}+65\,s$, is rapid, while the change in particle composition in the second regime, $t_{j,calc}+65\,s < t-t_j < t_{j+1}$, is slower. The first regime is significantly shorter but accounts for approximately 2/3 of the change in $X_{overall}$ during the carbonation period. The second regime comprises the majority of the time of the carbonation period, but only accounts for 1/3 of the change in $X_{overall}$.

At the beginning of the calcination period in each cycle, the particle briefly continues to carbonate before the onset of the calcination reaction. This brief amount of carbonation can be seen as a sharp dip in the overall reaction extent at the beginning of each cycle in Figure 4a. Increasing CO_2 concentration in the particle due to increasing surrounding CO_2 concentration elevates the transition temperature between the calcination and carbonation reactions. The transition temperature falls in the range 1100–1200 K, depending on the CO_2 concentration. The increasing CO_2 concentration and elevated transition temperature both prolong carbonation. For example, at the location $r/r_p=0.9$, $T=804.4\,K$ and $\bar{y}_{CO_2}=0.047$ at the beginning of cycle $j=4$, with a transition temperature of 993.8 K. The transition temperature for the location $r/r_p=0.9$ is reached after 5 s, when $T=1181.6\,K$ and $\bar{y}_{CO_2}=0.966$.

Local reaction extent for four selected locations within the particle is shown in Figure 5 for $j=4$. At the particle exterior, locations $r/r_p=1.0$ and $r/r_p=0.9$ begin the cycle with pure $CaCO_3$ ($X_{local}=0$) at $t=3300\,s$ and then completely calcine to CaO ($X_{local}=1$) at $t=3336\,s$ and $t=3364\,s$, respectively. Locations $r/r_p=0.8$ and $r/r_p=0.7$ begin the cycle at $t=3300\,s$ when $X_{local}=0.386$ and $X_{local}=0.687$, respectively and completely calcine to CaO at $t=3381\,s$ and $t=3390\,s$, respectively.

During the carbonation period, all locations return to their initial states, completely carbonated for $r/r_p=1.0$ and $r/r_p=0.9$ and partially carbonated for $r/r_p=0.8$ and $r/r_p=0.7$. After the carbonation period begins at $t=3600\,s$, the $r/r_p=1.0$ location only exhibits a rapid carbonation regime during the carbonation period. All other locations shown in Figure 5

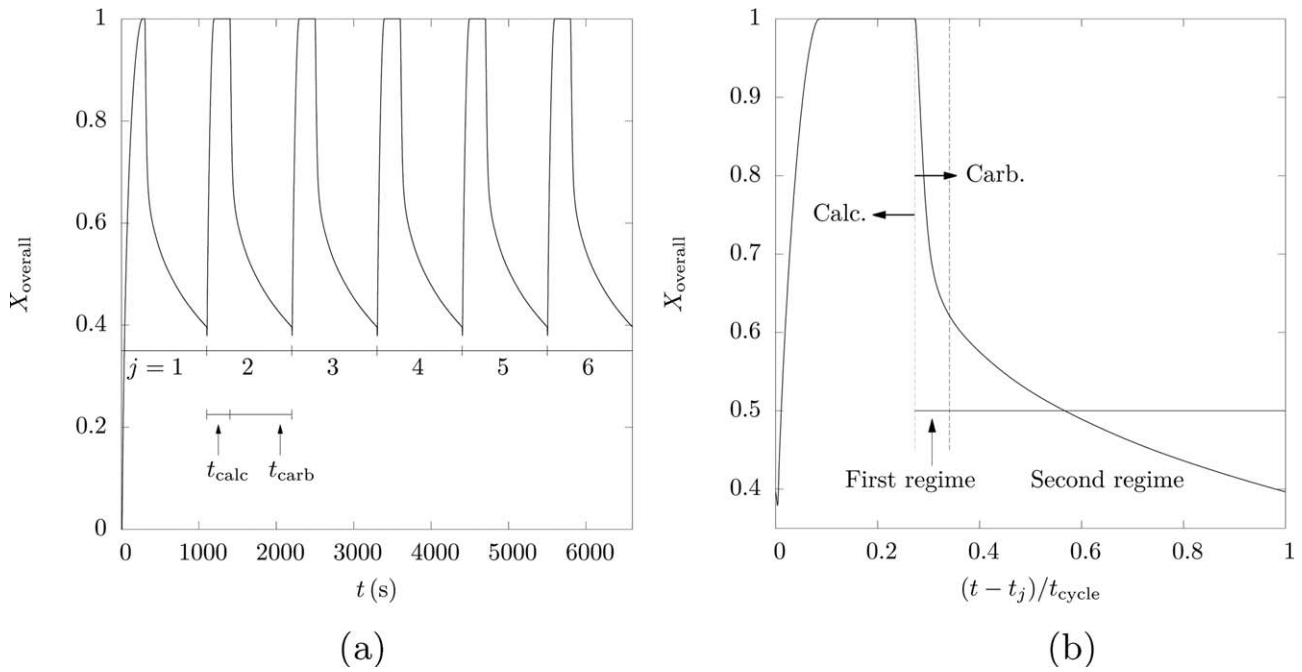

Figure 4. Overall reaction extent vs. time for the full-calcination case (a) undergoing six cycles and (b) for cycle $j = 4$.

exhibit both rapid and slower carbonation regimes, the second regime becoming longer with increasing distance from the particle surface.

After the calcination period, $X_{\text{local}} = 1$ at all locations in the particle. After the carbonation period, incomplete local carbonation at interior locations results in the maximum local carbonation extent and a non-uniform particle composition of a porous CaO core, a dense $CaCO_3$ outer shell, and a region of varying porosity between the two. During cycling, the particle transitions between these two states.

Figure 6 shows local temperature vs. time for cycle $j = 4$ for four selected locations within the particle. During the calcination period, three regions are observed. First, rapid heating of all locations when no chemical reaction occurs; second, a decrease in the rate of particle heating indicative of chemical reaction; and finally, temperature stagnation of all locations. The particle heats until calcination temperature is reached, at which point the surface of the particle begins reacting. Calcination is endothermic and therefore inhibits particle heating while the reaction proceeds. Heating inside the particle proceeds after calcination in the outer particle zone is complete. Once all locations have completely calcined, the particle is allowed to heat to a maximum temperature.

Three regions are also observed during the carbonation period. First, rapid particle cooling to the carbonation temperature; second, a decrease in the rate of particle cooling, indicative of the first, rapid carbonation regime, and finally, near-equilibrium temperature at all particle locations

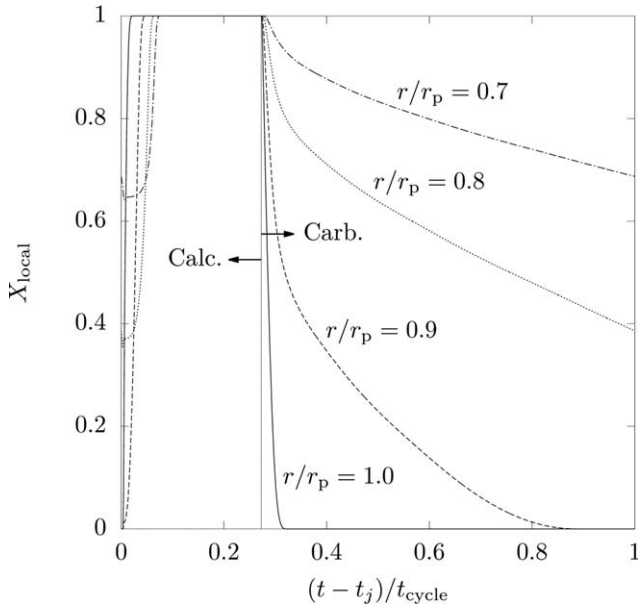

Figure 5. Local reaction extent vs. time for the full-calcination case for selected locations for cycle $j = 4$.

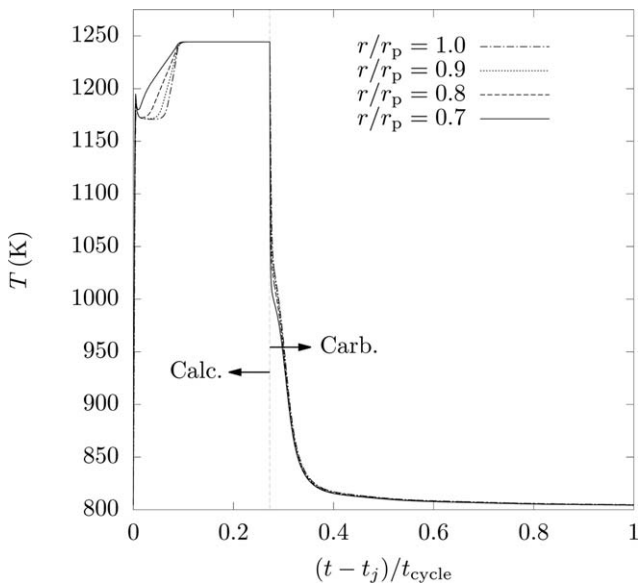

Figure 6. Local temperature vs. time for the full-calcination case for selected locations for cycle $j = 4$.

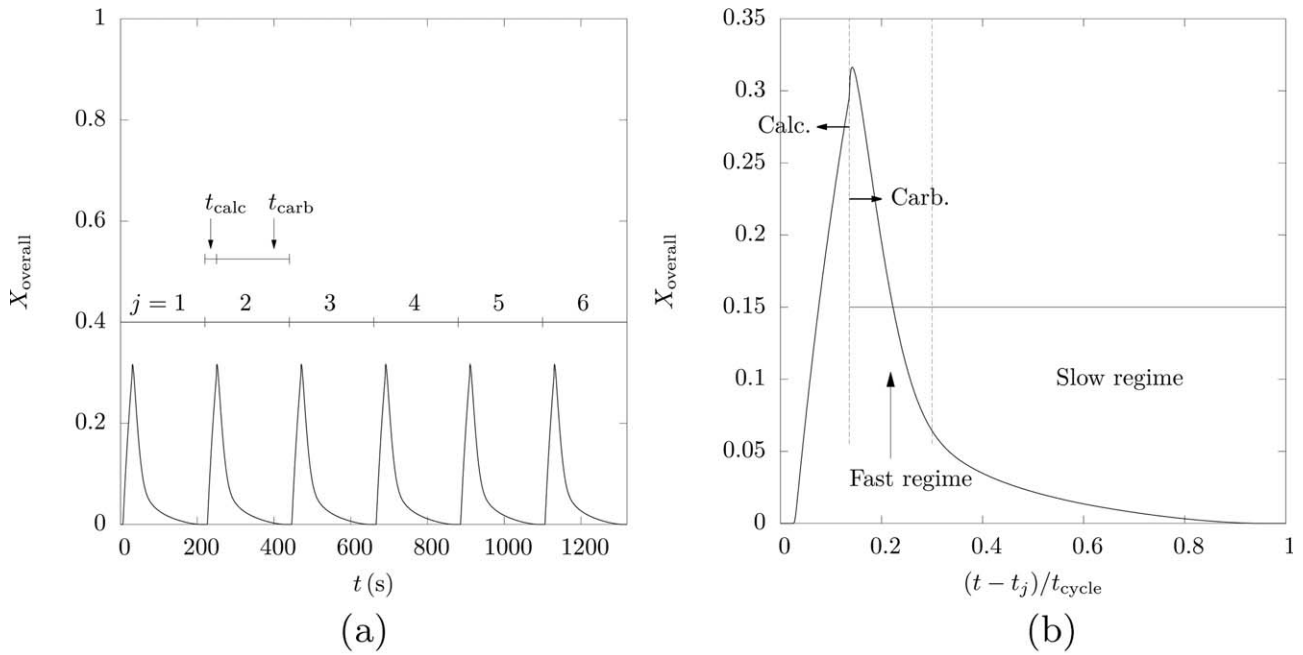

Figure 7. Overall reaction extent vs. time for the full-carbonation case (a) undergoing six cycles and (b) cycle $j = 4$.

indicative of the second, slower carbonation regime. Carbonation is exothermic and therefore slows particle cooling while the reaction proceeds. Exterior locations such as the particle surface reach lower temperatures earlier than interior locations. However, the differences in temperature between the locations during the carbonation period are smaller than the differences during the calcination period.

Full-carbonation case

Overall reaction extent vs. time is shown for the full-carbonation case in Figure 7. Figure 7a shows all six cycles, and Figure 7b shows cycle $j = 4$. The calcination periods start with particle heating to the calcination temperature. The calcination periods end at $t = t_j + 30$ s, corresponding to $X_{\text{overall}} = 0.298$. The following carbonation period proceeds until the particle is completely carbonated, $X_{\text{overall}} = 0$ at $t = t_{j+1}$. During the carbonation period, rapid and slower regimes are observed and are shown in Figure 7b. The rapid regime, $t_{j,\text{calc}} < t - t_j < t_{j,\text{calc}} + 30$ s, accounts for a larger fraction of the carbonation period time, 15.8% for the full-carbonation case vs. 8.1% for the full-calcination case. It also results in a larger change in X_{overall}, 71.8% for the full-carbonation case vs. 62.5% for the full-calcination case.

Local reaction extent for three selected locations in the particle for cycle $j = 4$ is shown in Figure 8. At the start of the calcination period at $t = 660$ s, all locations are at $X_{\text{local}} \approx 0$. When the calcination period begins, the particle surface $r/r_p = 1.0$ is the first location to reach the transition temperature and start calcining at $t = 666$ s. When the carbonation period starts, the $r/r_p = 1.0$ location immediately begins carbonating and continues to carbonate at a nearly constant rate until full carbonation is reached at $t = 744$ s. Locations near the particle surface begin calcining after the particle surface and only reach a partially calcined state. Locations $r/r_p = 0.9$ and $r/r_p = 0.8$ begin calcining at $t = 670$ s and $t = 672$ s, respectively. At the end of the calcination period at $t = 690$ s, locations $r/r_p = 0.9$ and $r/r_p = 0.8$ calcine to $X_{\text{local}} = 0.418$ and $X_{\text{local}} = 0.004$, respectively.

At the onset of the carbonation period at $t = 690$ s, locations where $X_{\text{local}} < 1$ briefly experience calcination before carbonation starts. Residual latent heat and the decrease in the transition temperature due to decreasing CO_2 concentrations extend calcination into the carbonation period until the temperature decreases below the transition temperature, and carbonation begins. Interestingly, the location $r/r_p = 0.9$ experiences the largest increase in local reaction extent, by 27%, when calcination occurs during the carbonation period, resulting in the maximum local reaction extent $X_{\text{local}} = 0.529$.

Locations $r/r_p < 0.9$ only experience a small amount of calcination during the calcination period. The location $r/r_p = 0.8$ has a local reaction extent of $X_{\text{local}} = 0.004$ at the end of the calcination period, and even lower values of X_{local} are observed for $r/r_p < 0.8$. After the calcination period, the particle composition is predominately a dense, unreacted

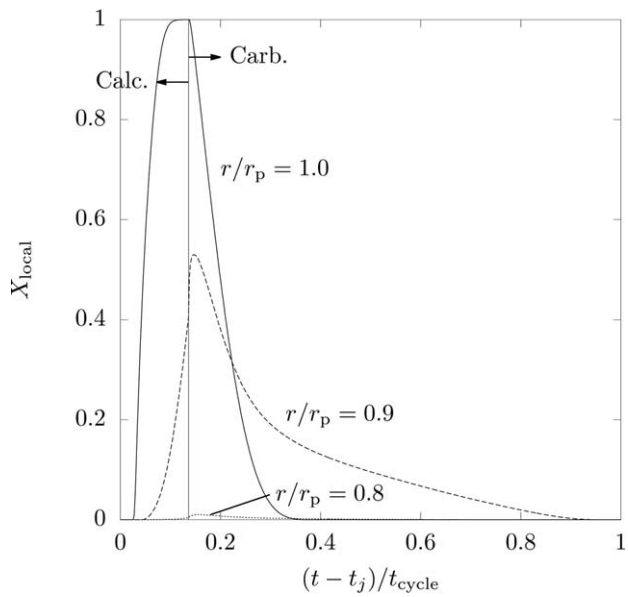

Figure 8. Local reaction extent vs. time for the full-carbonation cases for selected locations for cycle $j = 4$.

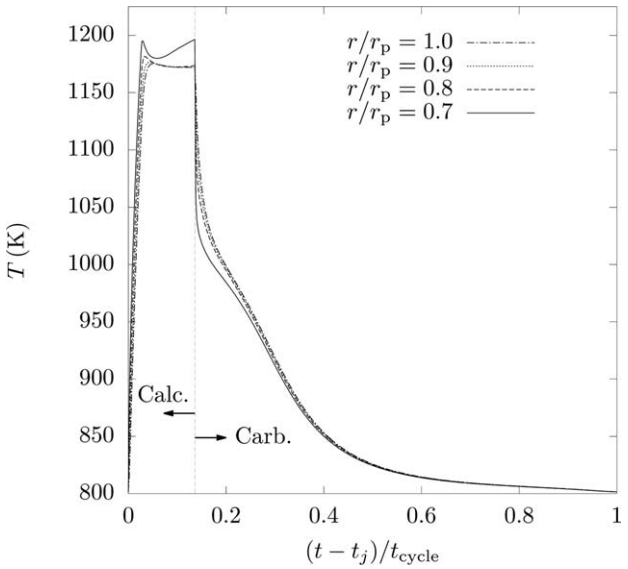

Figure 9. Local temperature vs. time for the full-carbonation case for selected locations for cycle $j = 4$.

$CaCO_3$ core, surrounded by a layer of porous CaO. After the carbonation period, the local reaction extent for all locations is nearly $X_{local}=0$. During cycling, the particle transitions between these two states.

Figure 9 shows local temperature vs. time for cycle $j = 4$ for four selected locations within the particle. During the calcination period, two regions are observed. First, a region of rapid particle heating at all locations, and then a region of decreased particle heating or no particle heating at all. All locations in the particle initially experience rapid heating without chemical reaction, then the calcination temperature is reached and chemical reaction begins, similar to the full-calcination case. Unlike the full-calcination case, the particle surface is the only location to completely calcine and experience a second period of heating during the calcination period. Other interior locations either only partially calcine or do not calcine at all, so the temperature of those locations remains relatively constant below the reaction temperature. The regions observed during the carbonation period of the full-carbonation case are similar to the regions observed in the full-calcination case: rapid particle cooling and periods indicative of the first, rapid and second, slower carbonation regimes.

Case comparison

The two cases are compared in terms of the relative amount of substance and mass of CO_2 captured for each cycle, referred to as the capture capacity

$$\bar{\xi}_c = \frac{N_{CO_2,cycle}}{N_{0,p}} \tag{27}$$

$$\xi_c = \frac{m_{CO_2,cycle}}{m_{0,p}} \tag{28}$$

where $N_{CO_2,cycle}$ and $m_{CO_2,cycle}$ are the amount of substance and mass of CO_2, respectively, absorbed by chemical reaction during the carbonation period only. The cases are also compared in terms of the theoretical energy required for regeneration of the carbonated sorbent relative to the incident energy, referred to as the energetic efficiency

Table 4. Case Comparison

Case	$\bar{\xi}_c$	ξ_c	η_e	$\bar{\chi}$ (μmol J^{-1})	χ (μg J^{-1})
Full-calcination	0.6034	0.2653	0.0336	0.1887	0.0083
Full-carbonation	0.2979	0.1310	0.1658	0.9316	0.0410

$$\eta_e = \frac{N_{CO_2,cycle}\bar{\Delta h}^0_{298\,K}}{Q_{surf,cycle}} \tag{29}$$

where $Q_{surf,cycle}$ is given by

$$Q_{surf,cycle} = \int_{t_j}^{t_{j+1}} \int_A q''_{surf}\, dA\, dt \tag{30}$$

Finally, the cases are compared in terms of the amount of substance and mass of CO_2 captured relative to the incident energy

$$\bar{\chi} = \frac{N_{CO_2,cycle}}{Q_{surf,cycle}} \tag{31}$$

$$\chi = \frac{m_{CO_2,cycle}}{Q_{surf,cycle}} \tag{32}$$

Values of these five metrics for the representative cycle $j = 4$ for the two cases are given in Table 4.

The full-calcination case has higher capture capacities than the full-carbonation case, because the particle is used more extensively to capture CO_2 in the full-calcination case. However, the full-carbonation case has higher energetic efficiency than the full-calcination case. A longer calcination period is required to fully calcine the particle, resulting in a higher solar energy input. For energetic efficiency of the full-calcination case, the increase in the amount of CO_2 captured does not outweigh the required higher solar energy input, resulting in the observed higher amounts of CO_2 captured per unit solar energy input for the full-carbonation case.

Summary

A numerical model coupling chemical kinetics, mass transfer, and heat transfer with time-periodic boundary conditions has been developed for a heterogeneous reacting particle. The thermochemical calcium oxide looping system was selected as the model reaction system because of its application in solar CO_2 capture. The model predicts the coupled transient transport phenomena and chemical reactions at the intra-particle level.

The model is used to investigate two cases: one in which full calcination is achieved and one in which full carbonation is achieved. Both systems reach periodicity after three cycles. In the full-calcination case, the maximum extent of calcination achieved at the end of the calcination period is $X_{overall}=1$, and the maximum extent of carbonation is achieved at the end of the carbonation period and corresponds to $X_{overall}=0.407$. In the full-carbonation case, the maximum extent of calcination achieved at the end of the calcination period is $X_{overall}=0.302$, and the maximum extent of carbonation is achieved at the end of the carbonation period, and corresponds to $X_{overall}=0$. In the full-calcination case, the core of the particle remains porous CaO during cycling, while in the full-carbonation case, the core of the particle remains dense $CaCO_3$ during cycling.

Calcination and carbonation period times were selected by trial and error to fulfill the target case conditions. Further

work will include calcination and carbonation period length optimization pertinent to sorbent particle size selection and solar reactor design optimization. Choice of period length is anticipated to be influenced by the reactor size and operation.

Notation

A = area, m^2
A_{eq} = equilibrium partial pressure pre-exponential factor, Pa
B_{eq} = equilibrium partial pressure constant, K
c = adsorption constant, $Pa^{-1/2}$
c_0 = adsorption constant pre-exponential factor, $Pa^{-1/2}$
D = diffusivity, $m^2\ s^{-1}$
E_a = activation energy, J mol^{-1}
E_c = adsorption constant energy, J mol^{-1}
f_{CO_2} = CO_2 partial pressure dependence
h = heat transfer coefficient, W $m^{-2}\ K^{-1}$
h_m = mass transfer coefficient, m s^{-1}
$\bar{h}$ = specific enthaply, J mol^{-1}
$\Delta\bar{h}^0_{298\,K}$ = enthalpy of reaction, J mol^{-1}
i = species index
j = cycle index
j''_{CO_2} = interphase molar flux, mol $m^{-2}\ s^{-1}$
k = reaction rate constant, mol $m^{-2}\ s^{-1}$
k_{eff} = effective thermal conductivity, W $m^{-1}\ K^{-1}$
k_0 = pre-exponential factor, mol $m^{-2}\ s^{-1}$
K = permeability, m^2
m = mass, kg
N = amount of substance, mol
p = pressure, Pa
q'' = radiative heat flux, W m^{-2}
Q = heat, J
r = radius or radial direction, m
$\bar{R}$ = universal gas constant, 8.314, J $mol\ K^{-1}$
$\bar{r}'''$ = volumetric reaction rate, mol $m^{-3}\ s^{-1}$
s = mass-specific reaction surface area, $m^2\ kg^{-1}$
s''' = volume-specific reaction surface area, m^{-1}
s'''_{phase} = interphase, volume-specific surface area, m^{-1}
t = time, s
T = temperature, K
u = velocity, m s^{-1}
V = volume, m^3
X = reaction extent
$\bar{y}$ = molar concentration

Greek symbols

α_{eff} = effective absorptivity
ε_{eff} = effective emissivity
η_e = energetic efficiency
θ = fraction of occupied active sites
μ = viscosity, N s m^{-2}
ξ_c = mass capture capacity
$\bar{\xi}_c$ = molar capture capacity
ρ = density, kg m^{-3}
$\bar{\rho}$ = molar density, mol m^{-3}
ϕ = porosity
χ = mass per energy input, μg J^{-1}
$\bar{\chi}$ = amount of substance per energy input, μmol J^{-1}

Subscripts

calc = calcination
carb = carbonation
eff = effective
eq = equilibrium
f = fluid
p = particle
rad = radiative
surf = surface
w = wall
0 = initial
∞ = surrounding

Superscripts

f = fluid phase
s = solid phase

Literature Cited

1. Stanmore B, Gilot P. Review—calcination and carbonation of limestone during thermal cycling for CO_2 capture. *Fuel Process Technol.* 2005;86:1707–1743.
2. Reich L, Yue L, Bader R, Lipiński W. Towards solar thermochemical carbon dioxide capture via calcium oxide looping: a review. *Aerosol Air Qual Res.* 2014;14:500–514.
3. Nikulshina V, Gálvez M, Steinfeld S. Kinetic analysis of the carbonation reactions for the capture of CO_2 from air via the $Ca(OH)_2$–$CaCO_3$–CaO solar thermochemical cycle. *Chem Eng J.* 2007;129:75–83.
4. Stalkup F. Carbon dioxide miscible flooding: past, present, and outlook for the future. *J Chem Petrochem Technol.* 1978;30:1102–1112.
5. Pierantozzi R. Carbon dioxide. In: *Kirk-Othmer Encyclopedia of Chemical Technology*. New York: Wiley, 2003.
6. Kim J, Miller J, Maravelias C, Stechel E. Comparative analysis of environmental impact of S2P (Sunshine to Petrol) system for transportation fuel production. *Appl Energy.* 2013;111:1089–1098.
7. Kim J, Johnson T, Miller J, Stechel E, Maravelias C. Fuel production from CO_2 using solar-thermal energy: system level analysis. *Energy Environ Sci.* 2012;5:8417–8429.
8. Ebner P, Lipiński W. Heterogeneous thermochemical decomposition of a semi-transparent particle under direct irradiation. *Chem Eng Sci.* 2011;66:2677–2689.
9. Ebner P, Lipiński W. Heterogeneous thermochemical decomposition of a semi-transparent particle under high-flux irradiation—changing grain size versus shrinking core models. *Numer Heat Transfer Appl.* 2012;62:412–431.
10. Takkinen S, Saastamoinen J, Hyppänen T. Heat and mass transfer in calcination of limestone particles. *AIChE J.* 2014;58:2563–2572.
11. Ebner P, Lipiński W. Heterogeneous thermochemical decomposition of a semi-transparent particle under high-flux irradiation: uniform versus non-uniform irradiation. *Heat Mass Transfer.* 2014;50:1031–1036.
12. Yue L, Lipiński W. A numerical model of transient thermal tranport phenomena in a high-temperature solid–gas reacting system for CO_2 capture applications. In: Proceedings of the 15th International Heat Transfer Conference, Kyoto, Japan, 2014:IHTC15–9014.
13. Lipiński W, Steinfeld A. Transient radiative heat transfer within a particle suspension undergoing endothermal decomposition—shrinking vs. non-shrinking particles. In: Proceedings of the 4th International Symposium on Radiative Transfer, Istanbul, Turkey, 2004.
14. Lipiński W, Steinfeld A. Heterogeneous thermochemical decomposition under direct irradiation. *Int J Heat Mass Transfer.* 2004;47:1907–1916.
15. Haussener S, Lipiński W, Petrasch J, Wyss P, Steinfeld A. Tomographic characterization of a semitransparent-particle packed bed and determination of its thermal radiative properties. *J Heat Transfer.* 2009;131:072701.
16. Dombrovsky L, Lipiński W. Transient temperature and thermal stress profiles in semi-transparent particles under high-flux irradiation. *Int J Heat Mass Transfer.* 2007;50:2117–2123.
17. Gallagher P, Johnson Jr. D. The effect of sample size and heating rate on the kinetics of the thermal decomposition of $CaCO_3$. *Thermochim Acta.* 1973;6:67–83.
18. Khinast J, Krammer G, Brunner C, Staudinger G. Decomposition of limestone: the influence of CO_2 and particle size on the reaction rate. *Chem Eng Sci.* 1996;51:623–634.
19. Bhatia S, Perlmutter D. Effect of the product layer on the kinetics of the CO_2-lime reaction. *AIChE J.* 1983;29:79–86.
20. Sun P, Grace J, Lim C, Anthony E. Determination of intrinsic rate constants of the CaO–CO_2 reaction. *Chem Eng Sci.* 2008;63:47–56.
21. Stendardo S, Foscolo P. Carbon dioxide capture with dolomite: a model for gas–solid reaction within the grains of a particulate sorbent. *Chem Eng Sci.* 2009;64:2343–2352.
22. Silcox G, Kramlich J, Pershling D. A mathematical model for the flash calcination of dispersed $CaCO_3$ and $Ca(OH)_2$ particles. *Ind Eng Chem Res.* 1989;28:155–160.
23. Mess D, Sarofim A, Longwell J. Product layer diffusion during the reaction of calcium oxide with carbon dioxide. *Energy Fuels.* 1999;13:999–1005.
24. García-Labiano F, Abad A, de Diego L, Gayán P, Adánez J. Calcination of calcium-based sorbents at pressure in a broad range of CO_2 concentrations. *Chem Eng Sci.* 2002;57:2381–2393.
25. Abanades J. The maximum capture efficiency of CO_2 using a carbonation/calcination cycle of CaO/$CaCO_3$. *Chem Eng J.* 2002;90:303–306.

26. Gupta H, Fan L. Carbonation–calcination cycle using high reactivity calcium oxide for carbon dioxide separation from flue gas. *Ind Eng Chem Res*. 2002;41:4035–4042.
27. Reich L, Bader R, Simon T, Lipiński W. Thermal transport model of a packed-bed reactor for solar thermochemical CO_2 capture. *Special Top Rev Porous Media*. 2015. In press.
28. Borgwardt R. Calcination kinetics and surface area of dispersed limestone particles. *AIChE J*. 1985;31:103–111.
29. Acharya B, Dutta A, Basu P. Circulating-fluidized-bed-based calcium-looping gasifier: experimental studies on the calcination-carbonation cycle. *Ind Eng Chem Res*. 2012;51:8652–8660.
30. Shimizu T, Hiramam T, Hosoda H, Kitano K, Inagaki M, Tejima K. A twin fluid-bed reactor for removal of CO_2 from combustion processes. *Chem Eng Res Design*. 1999;77:62–68.
31. Abanades J, Alvarez D. Conversion limits in the reaction of CO_2 with lime. *Energy Fuels*. 2003;17:308–315.
32. Kaviany M. *Principles of Heat Transfer in Porous Media*, 2nd ed. New York: Springer, 1995.
33. Manovic V, Anthony E. Sintering and formation of a nonporous carbonate shell at the surface of CaO-based sorbent particles during CO_2-capture cycles. *Energy Fuels*. 2010;24:5790–5796.
34. Barin I. *Thermochemical Data of Pure Substances*. Weinheim: VCH, 1989.
35. Lu D, Hughes R, Anthony E. Ca-based sorbent looping combustion for CO_2 capture in pilot-scale dual fluidized beds. *Fuel Process Technol*. 2008;89:1386–1395.

Manuscript received Jan. 15, 2015, and revision received Mar. 16, 2015.